PAPER

Check for updates

Shape complementarity processes for ultrashort-burst sensitive M13−PEG−WS$_2$-powered MCF-7 cancer cell sensors†

Maria P. Meivita, [ID] [a] Shao-Xiang Go,[a] Fitya S. Mozar,[a] Lunna Li,[b] Yaw Sing Tan, [ID] [c] Natasa Bajalovic [ID] *[a] and Desmond K. Loke [ID] *[a]

Biomarkers have the potential to be utilized in disease diagnosis, prediction and monitoring. The cancer cell type is a leading candidate for next-generation biomarkers. Although traditional digital biomolecular sensor (DBS) technology has shown to be effective in assessing cell-based interactions, low cell-population detection of cancer cell types is extremely challenging. Here, we controlled the electrical signature of a two-dimensional (2D) nanomaterial, tungsten disulfide (WS$_2$), by utilizing a combination of the Phage-integrated Polymer and the Nanosheet (PPN), *viz.*, the integration of the M13-conjugated polyethylene glycol (PEG) and the WS$_2$, through shape-complementarity phenomena, and developed a sensor system, *i.e.*, the Phage-based DBS (P-DBS), for the specific, rapid, sensitive detection of clinically-relevant MCF-7 cells. The P-DBS attains a detection limit of 12 cells per μL, as well as a contrast of 1.25 between the MCF-10A sample signal and the MCF-7 sample signal. A reading length of 200 μs was further achieved, along with a relative cell viability of ~100% for both MCF-7 and MCF-10A cells and with the PNN. Atomistic simulations reveal the structural origin of the shape complementarity-facilitated decrease in the output impedance of the P-DBS. The combination of previously unreported exotic sensing materials and digital sensor design represents an approach to unlocking the ultra-sensitive detection of cancer cell types and provides a promising avenue for early cancer diagnosis, staging and monitoring.

Introduction

Biomarkers have the ability to facilitate in disease monitoring, prediction and diagnosis.[1–3] When early detection is vital or diagnosis is challenging, there is a need to identify biomarkers that can be harnessed to determine diseases.[4–6] In the case of cancer, it is beneficial to discover biomarkers of the inflammatory process in addition to the qualitative and quantitative identification of cancer-specific biomarkers.[7–11] According to Brenner *et al.*, these biomarkers include acute-phase proteins, reactive oxygen and nitrogen species, immune-related effectors, cytokines or chemokines, mediators and prostaglandins, and cyclooxygenase-related factors.[12] The cancer cell type is a promising contender for next-generation biomarkers for

[a]Department of Science, Mathematics and Technology, Singapore University of Technology and Design, Singapore 487372, Singapore.
E-mail: natasa_bajalovic@sutd.edu.sg, desmond_loke@sutd.edu.sg
[b]Thomas Young Centre and Department of Chemical Engineering, University College London, London WC1E 7JE, UK
[c]Bioinformatics Institute, Agency for Science, Technology and Research (A*STAR), Singapore 138671, Singapore
†Electronic supplementary information (ESI) available. See DOI: https://doi.org/10.1039/d3nr03573e

applications in surveying treatment responses or unfavourable cases, diagnosis and toxicology.[13–15] Cancer cell detection at an ultrahigh degree of sensitivity is of critical importance for the early cancer diagnosis and monitoring.[16–18] However, cancer cell detection using traditional methods remains very difficult due to the small cancer cell population in specified samples.[19–21] Thence, the development of new strategies or sensing designs for cancer cell detection at low cell populations is required for clinical disease diagnosis.

Owing to difficulties in amplification, high costs, complicated operations and low sensitivity, the utilization of traditional cancer cell-detection approaches including quantitative real-time PCR, northern blotting and microarray-based hybridization has been limited in early diagnosis in clinical practice. The digital biomolecular sensor (DBS) technology has demonstrated to be favourable in examining cell-based interactions by analysing the current variation in a cancer cell element as a result of various advantages, such as rapid specific detection, low cost and high sensitivity.[22–26] However, due to the restricted number of cells in the cancer cell element, utilizing the conventional DBS scheme to detect cancer cells at low cell populations remains difficult. Thus, there is an urgent need to develop emerging material systems with high conductivity to enhance DBS performance. Many

next-generation two-dimensional (2D) nanosized materials have recently been investigated for cancer cell sensing, such as graphene, transition-metal dichalcogenides (TMDs), topological insulators, black phosphorus (BP) and MXenes.[27–31] However, owing to weak interactions with cancer cell types or low chemical stability, conventional 2D nanomaterials have specified limits. It is necessary to identify a novel 2D material with a strong cell-based interaction with cancer cell types.

Tungsten disulfide (WS_2) has intrigued the research community owing to its excellent physiochemical characters.[32,33] The WS_2 nanostructures, based on a hexagonal layer of tungsten atoms (M) sandwiched between two layers of sulfur atoms (X) in a stoichiometry MX_2, showing a layered configuration with strong covalent bonding within each layer and weak van der Waals forces between different MX_2 sheets, were created successfully through mechanical and chemical exfoliation strategies.[34,35] Additionally, WS_2 nanosheets have been utilized in phototransistors, photothermal therapy, thermophotovoltaic (TPV) cells and nonlinear optics.[36–38] Despite studies into the photothermal character of WS_2, the interaction between cancer cell types and nanostructures and the utility of a WS_2-based nanostructure in the digital sensing of cancer cells remain unclear.

The phage M13 is a cylindrical, ~880 nm long, and ~10 nm in diameter, non-lytic bacteriophage composed of specified proteins, capable of assembling on various cancer cells, such as ovarian cancer cells, colorectal cancer cells and prostate cancer cells.[39–42] Considering that: (i) the recognition-element component WS_2 discloses excellent electrical conductivity, enabling high cancer cell sensitivity, and (ii) another recognition-element component M13-conjugated polyethylene glycol (PEG) is utilized to coat the WS_2 nanostructure, which permits cancer cell-specific assembly, we postulate that the integration of the WS_2 and the M13-conjugated PEG may enable excellent recognition-element performance.

Herein, we modulate the electrical character of the WS_2 by harnessing the integration of the Phage-combined Polymer and the Nanosheet (the term PPN is utilized), *i.e.*, the incorporation of the M13-conjugated PEG and the WS_2, based on shape-complementarity effects, and design a sensor system, *viz.*, the Phage-based DBS (we call it P-DBS), for a specific, sensitive, rapid detection of clinically relevant MCF-7 cells. We developed a digital sensor system using a phage–nanosheet–polymer material platform for MCF-7 cells with a low detection limit, high contrast in output signals, along with a short reading time. The P-DBS discloses a detection limit of 12 cells per µL, together with a contrast of 1.25 between the MCF-7 sample signal and the MCF-10A sample signal. A relative cell viability of ~100% for both MCF-7 cells with PPNs and MCF-10A cells with the PPN was achieved, in addition to a reading length of 200 µs. Molecular dynamics (MD) simulations elucidate the structural basis of the output impedance decrease induced by shape-complementarity phenomena. The suggested scheme for cancer cell detection on the basis of the WS_2 material platform offers great potential for the creation of integrated lab-on-chip systems that can be utilized further in clinical settings (Fig. 1).
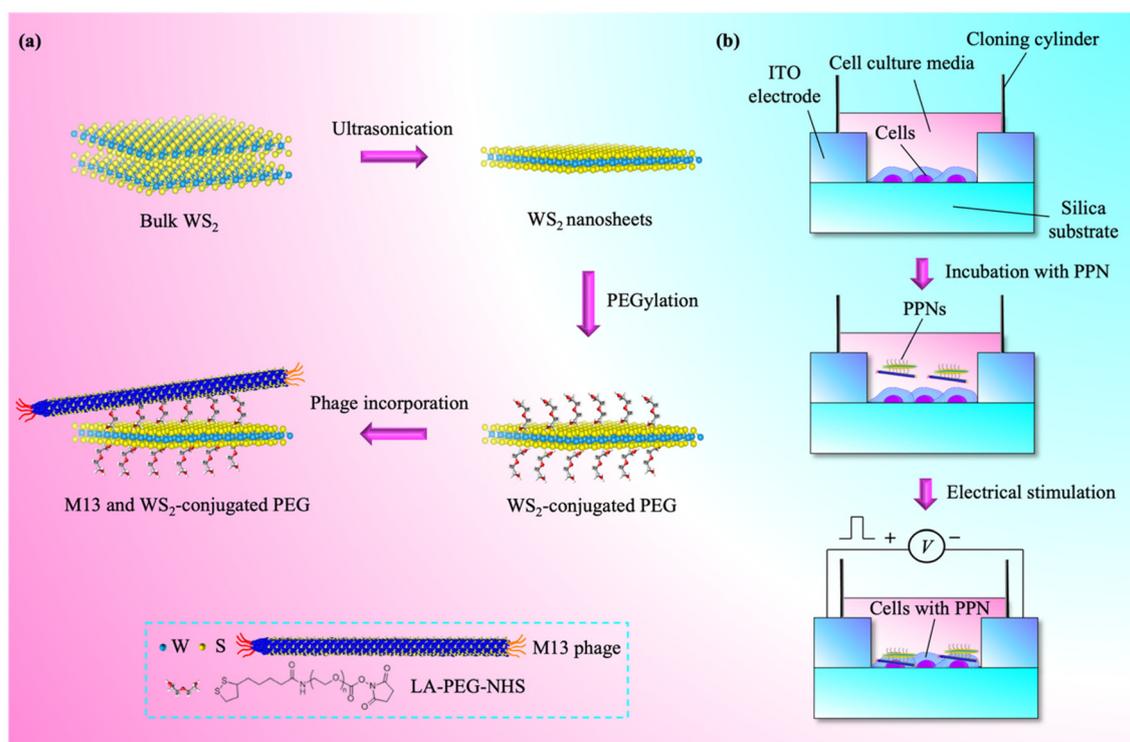

Fig. 1 A rapid sensitive DBS system based on the PPN. (a) Illustration of the WS_2−PEG synthesis and consequent phage conjugation. (b) Schematic representation of the P-DBS system. The PPN was incorporated in the DBS system for cancer cell detection.

Materials and methods

Molecular docking

The crystal structures of the N1 and N2 domains of the M13 bacteriophage minor-coat gene 3 protein (G3P) (PDB code, 1G3P[43]) and the extracellular domain of the human epidermal growth factor receptor 2 (HER2) bound to a nanobody (PDB code, 5MY6[44]) were obtained from the Protein Data Bank (PDB).[45] The oxidised Trp21 in the G3P structure was converted to an unmodified Trp. Missing loop residues in G3P and HER2 were modelled using the ModLoop web server.[46] G3P was docked to HER2 using the ClusPro[47] web server with default parameters. The top five docked models based on a balanced scoring scheme were visually inspected, and one was rejected as the binding interface was too small for the complex to be stable. The stability of the top-, third-, fourth-, and fifth-ranked models was further evaluated by MD simulations.

MD simulations

The C-termini of both proteins were capped by an N-methyl group. The protonation states of the residues were determined by the PDB2PQR software.[48] Each system was solvated with TIP3P water molecules[49] in a periodic truncated octahedron box such that its walls were at least 10 Å away from the proteins, followed by charge neutralization with sodium ions.

Four independent MD simulations using different initial atomic velocities were carried out on each of the four selected docked models. Energy minimization and MD simulations were performed with the PMEMD module of the Assisted Model Building with Energy Refinement (AMBER) 18[50] software using the ff14SB force field for the protein residues and the GLYCAM_06j-1[51] force field for the glycosylated asparagines and glycans. The SHAKE[52] algorithm was applied to constrain all bonds to hydrogen atoms, thus enabling a time step of 2 fs. Nonbonded interactions were truncated at 9 Å while electrostatic interactions were accounted for by the particle mesh Ewald method.[53] Energy minimization was carried out using the steepest descent algorithm for 1000 steps, followed by the conjugate gradient algorithm for another 1000 steps. The system was then gradually heated to 300 K over 50 ps at a constant volume before equilibration at a constant pressure of 1 atm for another 50 ps. Harmonic positional restraints with a force constant of 2.0 kcal mol^{-1} Å^{-2} were placed on the non-hydrogen atoms of the proteins during the energy minimization and equilibration steps. Subsequent unrestrained equilibration (2 ns) and production (300 ns) runs were carried out at 300 K and 1 atm. The Langevin thermostat[54] was utilized to maintain the temperature with a collision frequency of 2 ps^{-1}. Pressure was maintained by a Berendsen barostat[55] with a pressure relaxation time of 2 ps.

Binding free energy calculations

The binding free energies of the G3P-HER2 complexes were calculated using the Molecular Mechanics/Poisson–Boltzmann Surface Area (MM/PBSA) method[56] implemented in the AMBER 18 software.[50] Two hundred equally-spaced snapshot structures were extracted from the last 80 or 100 ns of the trajectories, and the molecular mechanical energies were calculated using the sander module. The polar contribution to the solvation free energy was calculated by the pbsa[57] program, with the solute dielectric constant set to 2 and the exterior dielectric constant set to 80. The nonpolar contribution was estimated from the solvent accessible surface area using the molsurf[58] program with $\gamma = 0.00542$ kcal Å^{-2} and $\beta = 0.92$.

The contribution of each residue to the binding free energy of the complex was computed by applying the free energy decomposition method[59] to two hundred equally-spaced structures extracted from the last 100 ns of the MD simulations on the fifth-ranked docked model. Binding free energies were calculated in the AMBER 18 software using the Molecular Mechanics/Generalized Born Surface Area (MM/GBSA) method.[56] The molecular-mechanical energies and the polar contribution to the solvation-free energy based on the modified Generalized Born (GB) model described by Onufriev et al.[60] were computed by the sander module. The nonpolar contribution to the solvation-free energy was estimated from the solvent-accessible surface area using the ICOSA method.[61]

Electrothermal simulation

The Ansys software was utilized to analyze the electric field distribution of the PPN cancer cell alternating current (AC) pulse sensor system using the finite-element method (FEM). The simulation parameters utilized were shown in ESI Table S3.† A reading stimulus in the 0.1–0.5 V range was applied to the system. The electric field was described by

$$E = R\{E(\omega)\exp(j\omega t)\}. \tag{1}$$

Cell culture

The breast cancer cells (MCF-7) were cultured in Dulbecco's modified Eagle's medium (DMEM) with L-glutamine (Nacalai Tesque) and 7% Fetal Bovine Serum (FBS) (Gibco), while the normal breast epithelial cells (MCF-10A) were cultured in a mixture of DMEM and Ham's F-12 (DMEM/F12). The DMEM/F12 was supplemented with 10% FBS (Gibco), 20 ng mL^{-1} epidermal growth factor (Gibco), 500 ng mL^{-1} hydrocortisone (Gibco), and 10 μg mL^{-1} insulin (Sigma). The MCF-7 and MCF-10A cells were maintained in a 37 °C incubator with 5% CO$_2$.

Escherichia coli (*E. coli*) and M13 bacteriophage propagation

The 5-alpha F'Iq competent *E. coli* (high efficiency) was purchased from New England Biolabs (NEB) as a host cell for propagating the M13 phage. An overnight culture (O.C.) of the *E. coli* was prepared using tetracycline (TET) and cultivated over 4–6 h on a 90 rpm shaker at 37 °C. The O.C. was utilized to inoculate the Lennox L Broth Base (LB Broth Base) and the LB Broth Base was incubated at 37 °C over 4–6 h until the optical density at 600 nm (OD$_{600}$) is 0.4. The M13 phage was purchased from the ATCC (15669-B1) and revived as per ATCC protocols. The first and second precipitations were performed

according to the ATCC M13 amplification protocol. The M13 bacteriophage concentrations were measured using a μDrop plate (Thermo Fisher Scientific).

PPN conjugation

The WS_2 nanosheets were sonicated from a bulk crystal suspended in sterile and deionized water (2D Semiconductors). Prior to the PPN conjugation, the sonicated WS_2 was PEGylated using the lipoic acid–polyethylene glycol–N-hydroxy-succinimide (LA–PEG–NHS) (Nanocs Inc.). For the PEG coating, the WS_2 was mixed with the LA–PEG–NHS on a shaker at 25 °C over 48 h. Filtered M13 phage was then added to the mixture and left to incubate for another 48 h at 25 °C under gentle shaking. The 0.22 μm-pore size filters were utilized to ensure the sterility of the phage. Finally, the conjugated PPN (WS_2/PEG/M13) was washed several times and resuspended in Dulbecco's Phosphate-Buffered Saline (DPBS).

Material characterization

The morphologies of the WS_2 and the PPN were investigated using atomic force microscopy (AFM, Bruker Dimension Icon system). Samples were drop-casted on the silicon (Si) substrate and examined using a 1.5 μm × 1.5 μm scan size. The sample thickness was measured using the Gwyddion software. The PPN was further characterized using transmission electron microscopy (TEM, FEI Talos F200 system) at an accelerating voltage of 120 kV. The TEM samples were prepared by negative staining and drop-casting the PPN on a carbon-coated Cu grid. Fourier-transform infrared spectroscopy (FTIR) of the WS_2, PEG, M13 and PPN was performed using a FTIR spectrometer (PerkinElmer) after drop-casting the samples on a Si substrate.

Cell cytotoxicity studies

MCF-7 and MCF-10A cells with a cell density of 3×10^3 cells per well were seeded in 96-well plates and incubated at 37 °C over 24 h. The medium was then removed from each well and different concentrations of WS_2 and PPN were added to the cells. The cells without the materials were used as an experimental control. The cells were incubated for another 24 h at 37 °C. The cytotoxicity of WS_2 and PPN was examined using the crystal violet (CV) staining assay. The materials were removed from each well, and the cells were washed twice with DPBS. The CV staining assay (50 μL per well) was added to the wells. The CV was then removed from the 96-well plates, dried overnight, and dissolved in 200 μL methanol. Finally, the optical density of the sample was measured at λ = 570 nm using a microplate absorbance reader (Thermo Scientific Multiskan GO).

Sensing evaluation

MCF-7 and MCF-10A cells were seeded on the indium tin oxide (ITO) subsystems utilized for the sensing experiments. In the subsystem, the left and right 650 nm-thick ITO electrodes were grown on a glass substrate (Latech). A cloning cylinder was then mounted on the substrate using a silicone adhesive (Sigma-Aldrich). The gap size between the electrodes was 100 μm. The MCF-7 and MCF-10A cells were plated in each subsystem at different seeding densities (1×10^3–7×10^3 cells per well) and incubated over 24 h. The PPN with a concentration of 10% was added to the subsystem. The cells without the PPN were harnessed as the experimental control. The cells were incubated for another 24 h at 37 °C. An arbitrary waveform generator (Tektronix Inc.) and a digital oscilloscope (Tektronix Inc.) were utilized to measure the output impedance. The pulse length in the 50–200 microsecond range and the sensing voltage in the 0.1–0.5 V range were harnessed.

Results

MD simulations

We docked the M13 minor coat protein, G3P, to the breast cancer cell protein HER2 using the ClusPro web server. Out of the top five docked models, four were selected for further evaluation in MD simulations. The unselected model exhibits a small binding interface, which likely results in a weak interaction. The G3P and HER2 proteins remained bound to each other in all the simulation runs of the four models. Based on the computed binding free energies obtained by the MM/PBSA method, the fifth-ranked docked model was the most stable (ESI Table S1†). We were unable to calculate the change in the conformational entropy as the system was too large for the normal mode analysis to be performed by the computer cluster utilized in this work. However, we note that the binding free energy value (this excludes the conformational entropy) for the G3P–HER2 complex (-107.2 kcal mol^{-1}) is much more favourable than the value we obtained previously for the G3P–PD-L1 complex (-72.5 kcal mol^{-1}).[75] The root-mean-square deviation of Cα atoms reaches a plateau in approximately the last 100 ns in all the simulation runs of the model (ESI Fig. S1†), indicating that the system is equilibrated and the complex has become stable.

The binding interface in the model is located at the N2 domain of the G3P and domains I and II of the HER2 (Fig. 2a). The proteins have a high shape complementarity at the binding interface, with the HER2 revealing a concave surface to match the convex surface of the G3P's N2 domain, thus allowing the HER2 to wrap around almost the entire G3P N2 domain. To examine which residues are important for the stability of the G3P–HER2 complex, we performed binding free energy decomposition based on the structures obtained from the MD simulations. The G3P residues, Arg162, Gln163, Trp199, Arg204, Phe208, Ser210, and Phe212 and the HER2 residues, Lys150, His257, Leu266, His267, Tyr274, Val308, Pro316, Lys333, and Arg351 contribute to most of the binding free energy (Fig. 2b–d). Hence, the complex is held together by a combination of hydrophobic interactions and polar interactions interspersed across the extensive binding interface. The breakdown of the components of the binding free energy calculated by the MM/PBSA scheme indicates that hydrophobic interactions contribute most significantly to complex formation (ESI Table S1†). These results suggest that the M13
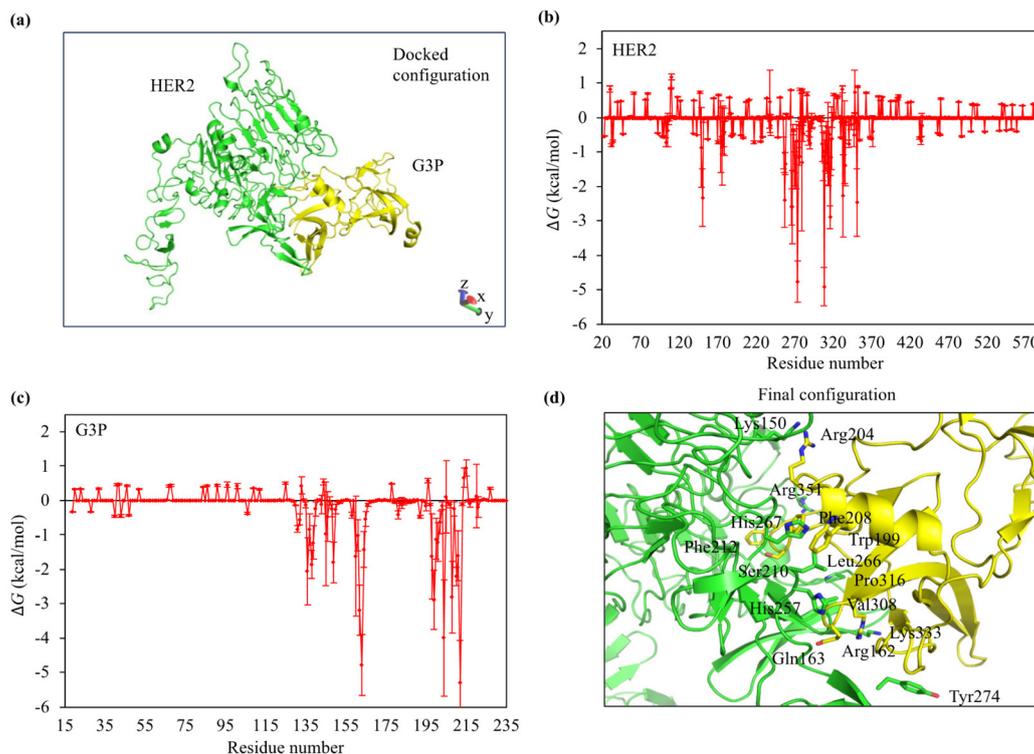
Fig. 2 Computational modelling of the G3P–HER2 interaction. (a) Snapshot of the docked model of the G3P–HER2 complex. G3P is shown in yellow, and HER2 is shown in green. (b) Binding free energy contributions of HER2 residues. (c) Binding free energy contributions of G3P residues. (d) Closeup snapshot of the binding interface of the G3P–HER2 complex obtained from the final trajectory frame of the simulation run with the most negative binding free energy (G3P in yellow, HER2 in green). The major interacting residues are shown as sticks.

phage may have enhanced affinity for breast cancer cells, which overexpress HER2 on the cancer cell surface, compared to that of healthy cells. In the case of the PPN, the concentration of the conductive WS_2 that assembles on cancer cells would be higher than that on healthy cells. Thus, when the DBS system is modified from DBS systems with MCF-10A cells and with the use of PPNs to the DBS system with MCF-7 cells and with the use of the PPN, a decreased output impedance would result.

Synthesis, characterization, and electrothermal simulations of PPN

Tungsten disulfide nanosheets in the PPN are generated by the ultrasonication-assisted liquid exfoliation of the bulk WS_2. We utilized atomic force microscopy (AFM) to characterize the WS_2 nanosheet. WS_2 nanosheets show an average lateral size of ~500 nm (Fig. 3a) and an average thickness of ~6 nm, as revealed by the AFM image, indicating a stack of two triple layers of WS_2 (Fig. 3b). To enhance stability and biocompatibility, we further modified the WS_2 nanosheet with PEG molecules.[62,63] Moreover, the M13 phage that selectively assembles on breast cancer cells was conjugated to PEG molecules to confer cancer cell targeting ability to WS_2 nanosheets.[64,65] The breast cancer cell protein HER2 is an attractive therapeutic target since it is a subtype of the integrin family that is unregulated in both angiogenic endothelial cells

and cancer cells.[66–68] The M13 phage and WS_2 nanosheets were conjugated to PEG molecules through the amine reaction and disulfide binding, respectively.[69,70] The conjugation was performed by utilizing the mixture of LA–PEG–NHS as a linker between the M13 phage and PEG molecules. The NHS of the LA–PEG–NHS reacts with the amine group on the M13 phage, while the LA binds to WS_2 nanosheets *via* disulfide binding. Finally, the PPN, *viz.*, the combination of the WS_2 and the M13-conjugated PEG, was prepared (Fig. 3c). To investigate the grafting of the LA–PEG–NHS on WS_2 nanosheets, Fourier-transform infrared (FTIR) spectroscopy was utilized (ESI Fig. S2†). The prototypical stretching vibration of the carbonyl group in the PEG at ~1090 cm^{-1} was revealed by the FTIR spectrum, which indicates the surface presence of PEG molecules.[71,72] The morphology of the PPN was examined by transmission electron microscopy (TEM). The TEM image disclosed that the PPN exhibited a flower-like morphology, as well as head- or sheet-type lateral size of ~400 nm (Fig. 3d). For pure WS_2 nanosheets, experiments in this work have revealed that the diameter of the WS_2 nanosheet is large (~500 nm). However, for the PPN, where the PEGylation was performed, the sonication process could partially break down the nanosheet, leading to a decrease in the diameter of WS_2 nanosheets.[73,74] The AFM image or cross-sectional plot shows that the average thickness of the PPN is ~30 nm (Fig. 3e and f), with an increase in the thickness as a result of the M13
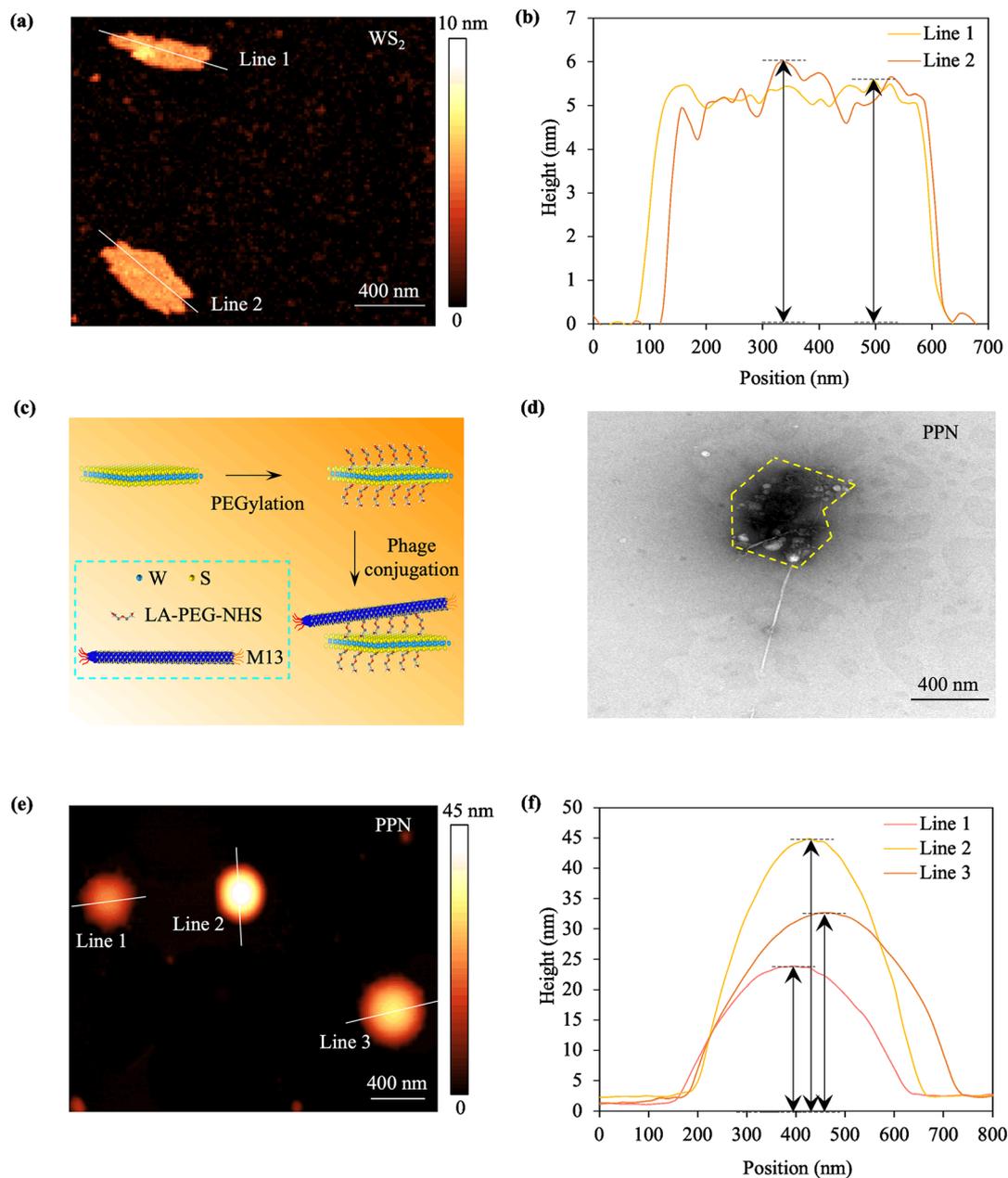
Fig. 3 PPN characterization. (a) AFM image of WS₂ nanostructures. (b) Height profiles of the WS₂ nanostructure along the white lines in (a). (c) An illustration revealing the PEGylation of WS₂ nanostructures and the subsequent phage-conjugation process. (d) Transmission electron microscopy (TEM) image of the PPN. The yellow dashed area comprises the head- or sheet-type structure. (e) Atomic force microscopy (AFM) image of the PPN. (f) Height profiles of the PPN, along the white lines in (e).

phage (~10 nm) and the PEG polymer coating (several nm).[75,76]

To examine the key point of the PPN for enhancing DBS performance, an electric-field simulation was implemented to investigate the influence of the PPN on the electrical signature of DBS systems. The reading stimuli were applied to the DBS configuration, and electric field distributions were recorded. The electric field distribution is revealed in ESI Fig. S3a,† in which a strong degree of electric field is observed in the cell layer and when the PPN is utilized. ESI Fig. S3b† discloses the

variation in the peak electric field for different reading voltages. The simulation findings indicate that the reading stimulus can modulate the electrical character of the DBS system with the PPN.

PPN phenomena for detecting cancer cells

The influence of the PPN on cytotoxicity was investigated. The cytotoxicity of WS₂ nanosheets is connected with surface processes.[77,78] To discern the cytotoxicity of a nanostructure, we define the degree of destructivity of the nanostructures as

nanostructure types. Thus, a change of the nanostructure type from the WS$_2$ nanosheet to the PPN corresponds to a smaller degree of destructivity. Since we are interested in the alteration in the extent of cytotoxicity of nanostructures, we record the variation in cell viability following the nanostructure addition. A marked dependence of the cell viability on the degree of destructivity and the material concentration was observed in Fig. 4a, b and ESI Fig. S4,† with a small degree of destructivity being the most suitable and a large degree of destructivity being the least suitable. When WS$_2$ nanosheets are utilized, the cell viability remains high for a low material concentration, *i.e.*, from 0–10%. In other words, nanostructures with a small degree of destructivity result in a low extent of cytotoxicity, so the nanostructure is non-cytotoxic. However, a decreased propensity in cell viability becomes conspicuous with increasing material concentrations, *viz.*, above 10%, owing to a decrease in the degree of destructivity. This means that a nanostructure with a high degree of destructivity could become cytotoxic. Moreover, a smaller degree of destructivity, *i.e.*, when the PPN is harnessed, should increase the material concentration allowed for achieving a targeted extent of cytotoxicity and render the nanostructure less cytotoxic.

To enhance the sensor sensitivity and induce nanostructure-specified cancer cell targeting or assembly, the M13 phage, which assembles on the HER2 overexpressed on a variety of cancer cells,[66–68] is integrated into the WS$_2$-conjugated PEG. We denote the degree of connectivity between nanostructures and cells as the cell type to understand the extent of assembly of the nanostructure on cells. Therefore, a lower degree of connectivity is represented by a modification in cell types from MCF-7 cells to MCF-10A cells. We examine the variation of the normalized impedance for different cell types, considering that we are curious about the alteration of the assembly character of nanostructures. The experiments in this work have demonstrated that cell samples, *i.e.*, MCF-7 cells with PPNs and MCF-10A cells with the PPN, exhibit an upper bound of the material concentration of 10% and a normalized cell viability of ∼100% (Fig. 4a and b). Similar normalized cell viability was also observed in the cells incubated with 10% PPN for both 0 h and 24 h in the experiment (ESI Fig. S5†). Based on these findings and to achieve high cell viability, a strong electrical conductivity, and a short incubation time, we utilized the PPN with a material concentration of ∼10% and an incubation time of 24 h. A clear dependence of the normalized impedance on the degree of connectivity and the variety of cell samples, *i.e.*, cells only or cells with nanostructures, is discerned in Fig. 4c and d, with a high degree of connectivity being the most effective and a low degree of con-
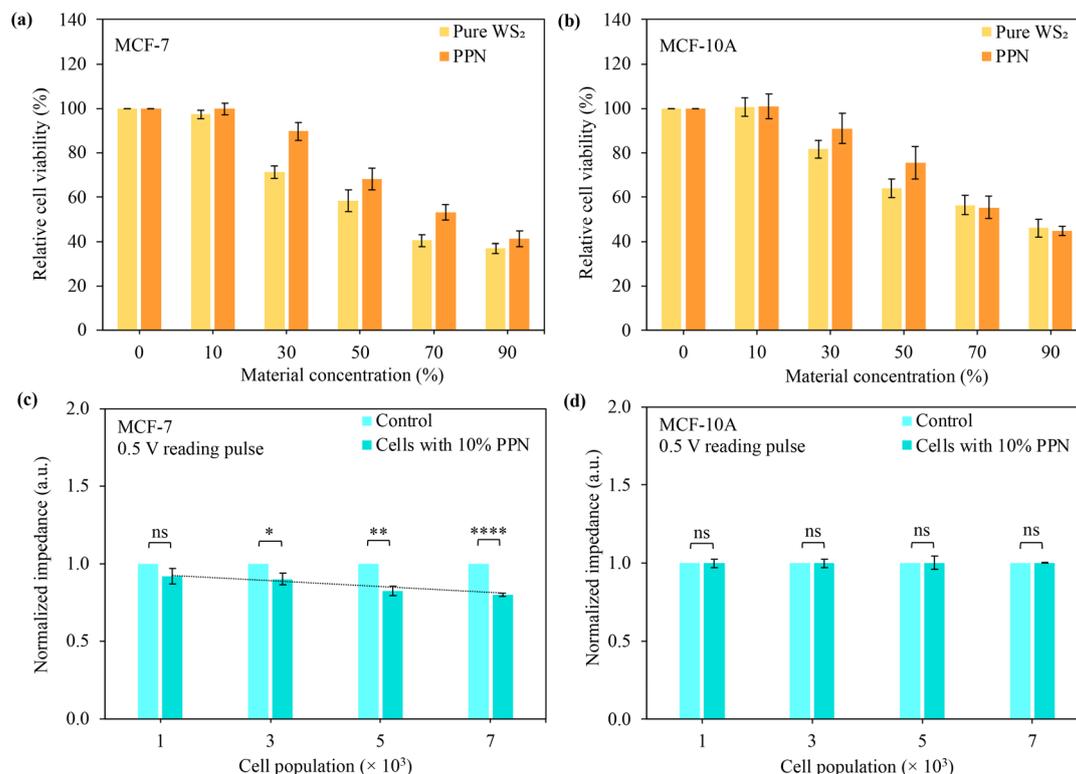

Fig. 4 Detecting MCF-7 cells using the P-DBS. (a and b) Variation of the normalized cell viability for different WS$_2$ and PPN concentrations for (a) MCF-7 and (b) MCF-10A cells. The statistical significance of relative cell viability can be found in supporting Table S2.† (c and d) Normalized impedance variations for different cell populations for (c) MCF-7 and (d) MCF-10A cells. The significance values were calculated utilizing the Student's *t*-test and were indicated as follows: non-significant (ns), $p \leq 0.05$ (*), $p \leq 0.01$ (**), and $p \leq 0.0001$ (****). Data are expressed as the standard error of the mean (SEM) where $n = 6$.

nectivity being the least effective. When pristine MCF-7 cells are utilized, the normalized impedance stays high. In other words, cell samples with a negligible or low degree of connectivity exhibit a minimal extent of assembly of the nanostructure on cells, so a negligible or small amount of nanostructures attach to cells. However, a downward trend in the normalized impedance becomes manifest as the cell sample variety is modified from MCF-7 cells only to MCF-7 cells with 10% PPN, owing to an increase in the degree of connectivity. This means that cell samples with a high degree of connectivity result, and a large amount of nanostructures attach to cells. Moreover, a low degree of connectivity appears when MCF-10A cells only or MCF-10A cells with PPNs are utilized.

An interesting phenomenon, associated with the assembly signature, was observed in the nanostructure. Experiments have disclosed that the output impedance of cells with nanostructures decreases with an increase in the stimulus amplitude owing to stronger electrostatic interactions between the nanostructure and cells.[79] The normalized impedance of MCF-7 cells with the PPN is determined for different reading amplitudes, and the results are shown in ESI Fig. S6a.† When an increased reading amplitude is applied, which means that nanostructures exhibit a high degree of connectivity, the nanostructure could be considered to attach to cells well, and a high strength of assembly of nanostructures on cells results. Furthermore, the normalized impedance decreases with an increase in the stimulus length (ESI Fig. S6b†), indicating an alterable nanostructure assembly character.

The calibration studies disclose that, for MCF-7 cells, the limit of detection (LOD) is ~12 cells per μL, *viz.*, the $LOD = 3.3 \times \frac{0.078}{0.022} = 12$, based on a linear-regression methodology.[79–81] The LOD is defined by the slope s of the linear plot of the normalized impedance as a function of the cell population, *i.e.*, the gradient of the dashed line in Fig. 4c, and the standard deviation σ of the normalized impedance.

$$LOD = 3.3 \times \left(\frac{\sigma}{s}\right) \qquad (2)$$

Recent studies have demonstrated a cell cycle analysis of MCF-7 cells, MCF-10A cells, and PANC-1 cells.[82–84] Cell population variations were observed in the cancer cells. Furthermore, among existing electrical-based cancer cell sensor types, *i.e.*, enzyme sensor, antibody sensor, nucleic acid sensor, and aptamer sensor, which have been implemented previously (ESI Fig. S7†), the phage-polymer-nanosheet based sensor utilized in this work and with the WS$_2$ and using a medium cell population has not been enacted before.

Discussion

Applications such as material design are particularly challenging for cancer cell detection because of several requirements: (1) high sensitivity, (2) marked contrast in output signals, (3) high cell viability, and (4) short reading time. Currently, none of the traditional electrical-based cancer cell sensors available fulfils all the requirements listed above. The examples shown in this work indicate that the current state of the P-DBS is able to achieve most of these requirements with reasonable sensitivity. The key improvement in the P-DBS system to enable these applications is the achievement of a LOD of 12 cells per μL, which is ~74% smaller than the average of 47 cells per μL for existing electrical-based cancer cell sensors using medium cell populations (ESI Fig. S8†). As a result, the detection of a small population of cancer cells is facilitated, and early disease diagnosis can be achieved. An excellent contrast in the output signal of the P-DBS was also obtained. The attainment of a contrast of 1.25 between the MCF-10A sample signal and the MCF-7 sample signal, *i.e.*, the ratio of the normalized impedance of MCF-10A cells with PPNs and with 7000 cells to that of MCF-7 cells with PPNs and with 7000 cells, $\frac{1.0}{0.8} = 1.25$, which is 58% larger than the average of ~0.79 for state-of-the-art electrical-based cancer cell sensors (ESI Fig. S9†), allows cancer cells to be distinguished well from healthy cells, facilitating early disease diagnosis. Another key advantage of the PNN is the cell viability attained. For example, both MCF-7 and MCF-10A cells with 10% PNN are able to achieve a relative cell viability of ~100%, which is 16 percentage points higher compared to the average of 84% for existing cancer cells with electrical sensor-based nanostructures (ESI Fig. S10†). This enables a large number of living cells to be maintained in a sample for accurate disease diagnosis. Another performance advantage can be achieved in terms of reading time. Recent studies disclose that the reading time is longer than that of the assembly kinetics, and this limits the overall operating time of traditional sensors.[85,86] A difficulty arises from the balance between decreasing the reading time and, at the same time, increasing the sensor LOD. In this work, the P-DBS discloses an alternating current (AC) reading length of 200 μs, which is ~150 times shorter compared to the average of ~30 ms for current electrical-based cancer cell sensors (ESI Fig. S11†). These allow cancer cells to be detected quickly, for achieving rapid disease diagnosis.

Conclusion

These high sensitivity, marked contrast in output signals, and short reading time are achieved through a shape-complementarity process in the P-DBS that alters the electrical signature of the WS$_2$. The LOD disclosed by the P-DBS is 12 cells per μL, which is 74% smaller than the average value for state-of-the-art electrical-based cancer cell sensors using a medium cell population. Moreover, the P-DBS exhibits a contrast of 1.25 between the MCF-10A sample signal and the MCF-7 sample signal, which is 58% higher than the average value of current electrical-based cancer cell sensors. An AC reading length of 200 μs in the P-DBS was also attained, which was 150 times shorter compared to the average value for existing electrical-based cancer cell sensors. Besides, both MCF-7 and MCF-10A cells with the PNN achieve a relative cell viability of ~100%, which

is 16 percentage points higher than the average value for current cancer cells with electrical sensor-based nano-structures. Furthermore, the structural basis of the shape-complementarity-enhanced decrease in the output impedance was elucidated by MD simulations. Thence, the proposed bio-molecular-sensor system depicts the first approach reported utilizing the PPN, *i.e.*, the integration of the WS_2 and the M13-conjugated PEG, and represents an exceptional opportunity for the design of lab-on-chip systems.

Data availability

The authors declare that data supporting the finding of this study are available within the article and the ESI.† Other data are available from the corresponding authors upon reasonable request.

Conflicts of interest

The authors declare no competing interests.

Acknowledgements

References

1 A. Chakraborty, S. Dasari, W. Long and C. Mohan, *Am. J. Cancer Res.*, 2019, **9**, 1104–1117.

2 A. Lokshin, R. C. Bast and K. Rodland, *Cancers*, 2021, **13**, 802.

3 T. M. Chanu, L. Kma and R. N. Sharan, *Indian J. Surg.*, 2023, 1–13.

4 P. Parasar, P. Ozcan and K. L. Terry, *Curr. Obstet. Gynecol. Rep.*, 2017, **6**, 34–41.

5 M. Bjerke and S. Engelborghs, *J. Alzheimer's Dis.*, 2018, **62**, 1199–1209.

6 D. Crosby, S. Bhatia, K. M. Brindle, L. M. Coussens, C. Dive, M. Emberton, S. Esener, R. C. Fitzgerald, S. S. Gambhir, P. Kuhn, T. R. Rebbeck and S. Balasubramanian, *Science*, 2022, **375**, eaay9040.

7 D. Çimen, N. Bereli and A. Denizli, *Biomed. Mater. Devices*, 2022, 1–11.

8 G. Pilvenyte, V. Ratautaite, R. Boguzaite, A. Ramanavicius, R. Viter and S. Ramanavicius, *Int. J. Mol. Sci.*, 2023, **24**, 4105.

9 J. Li, X. Feng, C. Zhu, Y. Jiang, H. Liu, W. Feng and H. Lu, *Front. Oncol.*, 2023, **13**, 1149599.

10 N. A. di Meo, D. Loizzo, S. D. Pandolfo, R. Autorino, M. Ferro, C. Porta, A. Stella, C. Bizzoca, L. Vincenti, F. Crocetto, O. S. Tataru, M. Rutigliano, M. Battaglia, P. Ditonno and G. Lucarelli, *Int. J. Mol. Sci.*, 2022, **23**, 4173.

11 M. del Pilar Chantada-Vázquez, A. C. López, M. G. Vence, S. Vázquez-Estévez, B. Acea-Nebril, D. G. Calatayud, T. Jardiel, S. B. Bravo and C. Núñez, *J. Proteomics*, 2020, **212**, 103581.

12 D. R. Brenner, D. Scherer, K. Muir, J. Schildkraut, P. Boffetta, M. R. Spitz, L. LeMarchand, A. T. Chan, E. L. Goode, C. M. Ulrich and R. J. Hung, *Cancer Epidemiol., Biomarkers Prev.*, 2014, **23**, 1729–1751.

13 M. P. Pavlou, E. P. Diamandis and I. M. Blasutig, *Clin. Chem.*, 2013, **59**, 147–157.

14 Q. Liu, C. Wu, H. Cai, N. Hu, J. Zhou and P. Wang, *Chem. Rev.*, 2014, **114**, 6423–6461.

15 A. M. Kabel, *J. Oncol. Sci.*, 2017, **3**, 5–11.

16 K. Wang, D. Fan, Y. Liu and E. Wang, *Biosens. Bioelectron.*, 2015, **73**, 1–6.

17 F. Ye, Y. Zhao, R. El-Sayed, M. Muhammed and M. Hassan, *Nano Today*, 2018, **18**, 103–123.

18 R. Liu, X. Ye and T. Cui, *Research*, 2020, 7949037.

19 L. Wu and X. Qu, *Chem. Soc. Rev.*, 2015, **44**, 2963–2997.

20 H. Kamali, S. Golmohammadzadeh, H. Zare, R. Nosrati, M. Fereidouni and H. Safarpour, *J. Nanobiotechnol.*, 2022, **20**, 438.

21 V. K. Sarhadi and G. Armengol, *Biomolecules*, 2022, **12**, 1021.

22 F. Cui, Z. Zhou and H. S. Zhou, *J. Electrochem. Soc.*, 2019, **167**, 037525.

23 A. Joshi, A. Vishnu G. K., T. Sakorikar, A. M. Kamal, J. S. Vaidya and H. J. Pandya, *Nanoscale Adv.*, 2021, **3**, 5542–5564.

24 D. Lee, S. S. Y. Chan, N. Aksic, N. Bajalovic and D. K. Loke, *ACS Omega*, 2021, **6**, 35325–35333.

25 D. Lee, J. S. Naikar, S. S. Y. Chan, M. P. Meivita, L. Li, Y. S. Tan, N. Bajalovic and D. K. Loke, *Nanoscale*, 2022, **14**, 7934–7942.

26 M. Li, F. Jiang, L. Xue, C. Peng, Z. Shi, Z. Zhang, J. Li, Y. Pan, X. Wang, C. Feng, D. Qiao, Z. Chen, Q. Luo and X. Chen, *Mol.*, 2022, **27**, 7327.

27 L. Wang, Q. Xiong, F. Xiao and H. Duan, *Biosens. Bioelectron.*, 2017, **89**, 136–151.

28 S. Kumar, Y. Lei, N. H. Alshareef, M. A. Quevedo-Lopez and K. N. Salama, *Biosens. Bioelectron.*, 2018, **121**, 243–249.

29 S. S. Y. Chan, Y. S. Tan, K.-X. Wu, C. Cheung and D. K. Loke, *ACS Appl. Bio Mater.*, 2018, **1**, 210–215.

30 C. Huang, S. Hu, X. Zhang, H. Cui, L. Wu, N. Yang, W. Zhou, P. K. Chu and X.-F. Yu, *Biosens. Bioelectron.*, 2020, **165**, 112384.

31 S. S. Y. Chan, D. Lee, M. P. Meivita, L. Li, Y. S. Tan, N. Bajalovic and D. K. Loke, *Nanoscale Adv.*, 2021, **3**, 6974–6983.

32 S. Roy and P. Bermel, *Sol. Energy Mater. Sol. Cells*, 2018, **174**, 370–379.

33 J. Ding, A. Feng, X. Li, S. Ding, L. Liu and W. Ren, *J. Phys. Appl. Phys.*, 2021, **54**, 173002.

34 L. Cheng, J. Liu, X. Gu, H. Gong, X. Shi, T. Liu, C. Wang, X. Wang, G. Liu, H. Xing, W. Bu, B. Sun and Z. Liu, *Adv. Mater.*, 2014, **26**, 1886–1893.

35 S. Wang, J. Zhao, H. Yang, C. Wu, F. Hu, H. Chang, G. Li, D. Ma, D. Zou and M. Huang, *Acta Biomater.*, 2017, **58**, 442–454.

36 N. Huo, S. Yang, Z. Wei, S.-S. Li, J.-B. Xia and J. Li, *Sci. Rep.*, 2014, **4**, 5209.

37 X.-Z. Cui, Z.-G. Zhou, Y. Yang, J. Wei, J. Wang, M.-W. Wang, H. Yang, Y.-J. Zhang and S.-P. Yang, *Chin. Chem. Lett.*, 2015, **26**, 749–754.

38 J.-T. Wang, W. Zhang, W.-B. Wang, Y.-J. Wu, L. Zhou and F. Cao, *Biochem. Biophys. Res. Commun.*, 2019, **511**, 587–591.

39 I. Kim, J.-S. Moon and J.-W. Oh, *Nano Converg.*, 2016, **3**, 27.

40 J. S. Moon, E. J. Choi, N. N. Jeong, J. R. Sohn, D. W. Han and J. W. Oh, *Nanomaterials*, 2019, **9**, 1448.

41 D. K. Loke, G. J. Clausen, J. F. Ohmura, T.-C. Chong and A. M. Belcher, *ACS Appl. Nano Mater.*, 2018, **1**, 6556–6562.

42 C. Chang, W. Guo, X. Yu, C. Guo, N. Zhou, X. Guo, R.-L. Huang, Q. Li and Y. Zhu, *Mater. Today Bio*, 2023, **20**, 100612.

43 J. Lubkowski, F. Hennecke, A. Plückthun and A. Wlodawer, *Nat. Struct. Biol.*, 1998, **5**, 140–147.

44 M. D'Huyvetter, J. De Vos, C. Xavier, M. Pruszynski, Y. G. J. Sterckx, S. Massa, G. Raes, V. Caveliers, M. R. Zalutsky, T. Lahoutte and N. Devoogdt, *Clin. Cancer Res.*, 2017, **23**, 6616–6628.

45 H. M. Berman, J. Westbrook, Z. Feng, G. Gilliland, T. N. Bhat, H. Weissig, I. N. Shindyalov and P. E. Bourne, *Nucleic Acids Res.*, 2000, **28**, 235–242.

46 A. Fiser and A. Sali, *Bioinformatics*, 2003, **19**, 2500–2501.

47 D. Kozakov, D. R. Hall, B. Xia, K. A. Porter, D. Padhorny, C. Yueh, D. Beglov and S. Vajda, *Nat. Protoc.*, 2017, **12**, 255–278.

48 T. J. Dolinsky, P. Czodrowski, H. Li, J. E. Nielsen, J. H. Jensen, G. Klebe and N. A. Baker, *Nucleic Acids Res.*, 2007, **35**, W522–W525.

49 W. L. Jorgensen, J. Chandrasekhar, J. D. Madura, R. W. Impey and M. L. Klein, *J. Chem. Phys.*, 1983, **79**, 926–935.

50 D. A. Case, I. Y. Ben-Shalom, S. R. Brozell, D. S. Cerutti, T. E. III, V. W. D. Cruzeiro, T. A. Darden, R. E. Duke, D. Ghoreishi, M. K. Gilson, H. Gohlke, A. W. Goetz, D. Greene, R. Harris, N. Homeyer, Y. Huang, S. Izadi, A. Kovalenko, T. Kurtzman, T. S. Lee, S. LeGrand, P. Li, C. Lin, J. Liu, T. Luchko, R. Luo, D. J. Mermelstein, K. M. Merz, Y. Miao, G. Monard, C. Nguyen, H. Nguyen, I. Omelyan, A. Onufriev, F. Pan, R. Qi, D. R. Roe, A. Roitberg, C. Sagui, S. Schott-Verdugo, J. Shen, C. L. Simmerling, J. Smith, R. Salomon-Ferrer, J. Swails, R. C. Walker, J. Wang, H. Wei, R. M. Wolf, X. Wu, L. Xiao, D. M. York and P. A. Kollman, University of California, San Francisco, 2018..

51 K. N. Kirschner, A. B. Yongye, S. M. Tschampel, J. Gonzalez-Outeirino, C. R. Daneils, B. L. Foley and R. J. Woods, *J. Comput. Chem.*, 2008, **29**, 622–655.

52 J.-P. Ryckaert, G. Ciccotti and H. J. C. Berendsen, *J. Comput. Phys.*, 1977, **23**, 327–341.

53 T. Darden, D. York and L. Pedersen, *J. Chem. Phys.*, 1993, **98**, 10089–10092.

54 J. A. Izaguirre, D. P. Catarello, J. M. Wozniak and R. D. Skeel, *J. Chem. Phys.*, 2001, **114**, 2090–2098.

55 H. J. C. Berendsen, J. P. M. Postma, W. F. van Gunsteren, A. DiNola and J. R. Haak, *J. Chem. Phys.*, 1984, **81**, 3684–3690.

56 J. Srinivasan, T. E. Cheatham, P. Cieplak, P. A. Kollman and D. A. Case, *J. Am. Chem. Soc.*, 1998, **120**, 9401–9409.

57 R. Luo, L. David and M. K. Gilson, *J. Comput. Chem.*, 2002, **23**, 1244–1253.

58 M. L. Connolly, *J. Appl. Crystallogr.*, 1983, **16**, 548–558.

59 H. Gohlke, C. Kiel and D. A. Case, *J. Mol. Biol.*, 2003, **330**, 891–913.

60 A. Onufriev, D. Bashford and D. A. Case, *Proteins*, 2004, **55**, 383–394.

61 M. Rarey, B. Kramer, T. Lengauer and G. Klebe, *J. Mol. Biol.*, 1996, **261**, 470–489.

62 N. Kong, L. Ding, X. Zeng, J. Wang, W. Li, S. Shi, S. T. Gan, X. Zhu, W. Tao and X. Ji, *Nanophotonics*, 2019, **8**, 2331–2346.

63 M. P. Meivita, S. S. Y. Chan, S. X. Go, D. Lee, N. Bajalovic and D. K. Loke, *ACS Omega*, 2022, **7**, 23075–23082.

64 B. Cao, M. Yang and C. Mao, *Acc. Chem. Res.*, 2016, **49**, 1111–1120.

65 J. Wang, A. Lamolinara, L. Conti, M. Giangrossi, L. Cui, M. B. Morelli, C. Amantini, M. Falconi, C. Bartolacci, C. Andreani, F. Orlando, M. Provinciali, F. D. Del Pizzo, F. Russo, B. Belletti, F. Riccardo, E. Bolli, E. Quaglino, F. Cavallo, A. Amici, M. Iezzi and C. Marchini, *Cancers*, 2022, **14**, 4054.

66 R. Kumar and R. Yarmand-Bagheri, *Semin. Oncol.*, 2001, **28**, 27–32.

67 W. Tai, R. Mahato and K. Cheng, *J. Controlled Release*, 2010, **146**, 264–275.

68 N. Iqbal and N. Iqbal, *Mol. Biol. Int.*, 2014, **2014**, 852748.

69 W.-J. Chung, D.-Y. Lee and S. Y. Yoo, *Int. J. Nanomed.*, 2014, **9**, 5825–5836.

70 W. Feng, L. Chen, M. Qin, X. Zhou, Q. Zhang, Y. Miao, K. Qiu, Y. Zhang and C. He, *Sci. Rep.*, 2015, **5**, 17422.

71 I. M. Deygen and E. V. Kudryashova, *Colloids Surf., B*, 2016, **141**, 36–43.

72 A. Kumar, M. O. Shaikh, R. R. Kumar, K. Dutt, C. T. Pan and C. H. Chuang, *Nanoscale*, 2022, **14**, 1742–1754.

73 J. T. Robinson, S. M. Tabakman, Y. Liang, H. Wang, H. Sanchez Casalongue, D. Vinh and H. Dai, *J. Am. Chem. Soc.*, 2011, **133**, 6825–6831.

74 M. H. Shariare, A.-A. Masum, S. Alshehri, F. K. Alanazi, J. Uddin and M. Kazi, *Molecules*, 2021, **26**, 1457.

75 M. P. Meivita, D. Lee, J. S. Naikar, S.-X. Go, W. C. Teoh, Y. S. Tan, N. Bajalovic and D. K. Loke, *Pharmaceutics*, 2023, **15**, 106.

76 L. Shi, J. Zhang, M. Zhao, S. Tang, X. Cheng, W. Zhang, W. Li, X. Liu, H. Peng and Q. Wang, *Nanoscale*, 2021, **13**, 10748–10764.

77 J. H. Appel, D. O. Li, J. D. Podlevsky, A. Debnath, A. A. Green, Q. H. Wang and J. Chae, *ACS Biomater. Sci. Eng.*, 2016, **2**, 361–367.

78 W. Z. Teo, E. L. K. Chng, Z. Sofer and M. Pumera, *Chem. – Eur. J.*, 2014, **20**, 9627–9632.

79 D. Lee, S. S.-Y. Chan, J. S. Naikar, M. P. Meivita, W.-C. Teoh, N. Bajalovic and D. K. Loke, *Mater. Adv.*, 2023, **4**, 291–301.

80 S. Forouzanfar, F. Alam, N. Pala and C. Wang, *Biosens. Bioelectron.*, 2020, **170**, 112598.

81 X. Xu, J. Ji, P. Chen, J. Wu, Y. Jin, L. Zhang and S. Du, *Anal. Chim. Acta*, 2020, **1125**, 41–49.

82 P. J. Pak, D. G. Lee, J. H. Sung, S. H. Jung, T.-Y. Han, S. H. Park and N. Chung, *Mol. Med. Rep.*, 2021, **23**, 1–9.

83 S. Jose, T. A. Cinu, R. Sebastian, M. H. Shoja, N. A. Aleykutty, A. Durazzo, M. Lucarini, A. Santini and E. B. Souto, *Polymers*, 2019, **11**, 1905.

84 J. B. Foo, L. S. Ng, J. H. Lim, P. X. Tan, Y. Z. Lor, J. S. E. Loo, M. L. Low, L. C. Chan, C. Y. Beh, S. W. Leong, L. S. Yazan, Y. S. Tor and C. W. How, *RSC Adv.*, 2019, **9**, 18359–18370.

85 J. L. Arlett, E. B. Myers and M. L. Roukes, *Nat. Nanotechnol.*, 2011, **6**, 203–215.

86 G. Ertürk, H. Özen, M. A. Tümer, B. Mattiasson and A. Denizli, *Sens. Actuators, B*, 2016, **224**, 823–832.